

Coupled poro-elastic behavior of hyper-elastic membranes

Alexander Gehrke^a, Zoe King^a, Kenneth S. Breuer^{a,*}

^a*School of Engineering, Brown University, 182 Hope Street, Providence, 02912, Rhode Island, United States of America*

Abstract

This study investigates the coupled deformation and flow behavior through thin, hyper-elastic, porous membranes subjected to pressure loading. Using bulge test experiments, optical deformation measurements, and flow rate characterization, we analyze the structural and fluid dynamic responses of membranes with varying material stiffness and porosity patterns. A two-parameter Gent model captures the hyper-elastic deformation, while local stretch analyses reveal the evolution of pore sizes across the membrane. We find that membrane stretch is primarily governed by material stiffness and applied pressure, independent of porosity. A gradient of increasing pore size toward the membrane center emerges due to higher local stretch, while the total open pore area remains approximately constant across radial layers of the membrane. Flow rate scaling is characterized using a discharge coefficient that accounts for pore area expansion and pressure losses. While the initial scaling compares well in most cases, it breaks down for scenarios with significantly different pore Reynolds numbers, driven by large variations in initial porosity. To address this, we introduce a Reynolds-dependent correction term that unifies discharge coefficient predictions across diverse porosity and flow velocity conditions. These findings enhance the understanding of poro-elastic systems and provide robust scaling relationships for designing thin, flexible, porous structures in applications such as bio-inspired aerodynamic systems and adaptive flow regulation devices.

Keywords: Poro-elastic membranes, Fluid-structure interaction, Hyper-elastic deformation, Discharge coefficient

*Corresponding author. E-mail address: kenneth_breuer@brown.edu

1. Introduction

Poro-elastic materials combine flexibility with porosity, and are widespread in both natural and engineered systems across a large range of length scales. In nature, they are found in plant structures like leaves and seeds, or trees, which use the porosity to reduce structural loads (Vogel, 1984, 1989) or efficient seed dispersal (Cummins et al., 2018). Similarly, the bristled wings of tiny insects and bird feathers employ porosity to enhance aerodynamic performance, by being lightweight and resilient enabling efficient (Eberle et al., 2014; Santhanakrishnan et al., 2014; Kolomenskiy et al., 2020; Jiang et al., 2022) and silent flight (Jaworski and Peake, 2013, 2020). Agglomerations of individual non-porous bundles can act as poro-elastic terrestrial (Brunet, 2020) and aquatic (Nepf, 2012) canopies even when individual blades or leaves are non-porous.

In engineering, poro-elastic materials are critical for applications ranging from rock mechanics to tissue engineering and medical devices. For instance, poro-elasticity plays a crucial role in the mechanics of porous rock sediments for modeling subsurface fluid flow (Detournay, 1993; Steeb and Renner, 2019). In the medical field, the study of poro-elastic properties in bones (Ehret et al., 2017) and living tissues (Nia et al., 2011; Malandrino and Moendarbary, 2019) has informed the development of implants and other medical devices. Moreover, soft elastomeric materials are increasingly used in applications like soft robotics (Shian et al., 2015; Whitesides, 2018; Jones et al., 2021), medical (Roche et al., 2014), and bio-inspired engineering (Song et al., 2008; Gehrke et al., 2022; Gehrke and Mulleners, 2025), due to their ability to undergo large deformations while maintaining their structural integrity (Michel et al., 2010).

Despite significant progress in fluid-structure interaction modeling (Dowell and Hall, 2001; Venkataraman et al., 2014), the role of poro-elastic interactions, especially in the context of inertia, remains underexplored (Tiomkin and Raveh, 2021). This is particularly evident in aerodynamics, where porosity can significantly impact the performance and efficiency of various structures, such as parachutes (Heinrich and Haak, 1971; Kim and Peskin, 2006; Kanai et al., 2019), porous airfoils (Geyer et al., 2010; Aldheeb et al., 2018), and sails (Murata and Tanaka, 1989). While there is a particular gap in experimental poro-elastic studies significant effort has been made in the the-

oretical modeling (Iosilevskii, 2011, 2013; Baddoo et al., 2021), and individual studies of the effect of compliant membranes (Song et al., 2008; Mathai et al., 2023) and porous screens (Pinker and Herbert, 1967; Castro, 1971; Koo and James, 1973; Cummins et al., 2017).

This paper focuses on the experimental characterization of large deformations and flow rate through highly flexible poro-elastic membranes under different pressure loadings. Building on the work of (Das et al., 2020), we fabricate membranes with varying material strengths and porosity patterns, employing a fabrication process that allows for precise control of mechanical properties and pore distribution. By subjecting these membranes to controlled pressure conditions, we gain new insights into the complex fluid-structure interactions governing their response. Our methods include optical deformation measurements, local stretch analysis to capture pore size variation along the membrane, and flow rate measurements through the open pores to characterize the discharge.

We integrate a two-parameter Gent model for the deformation scaling and extend it to determine the pore-size evolution across the membrane. Combining the two models allows us to predict the three-dimensional shape of the membranes and its pore size distribution for varying pressure loading. By defining a pore discharge coefficient, we establish a scaling ratio that captures the relationship for all measured flow rates of different material strengths and porosity patterns.

This study advances our understanding of poro-elastic membranes and provides practical guidelines for the application of porous fluid-structure interaction systems, e.g. in bio-inspired aerodynamic designs. Our research contributes to the broader understanding of poro-elastic materials and their applications in both natural and engineered systems. The methodologies and findings presented here are expected to pave the way for future research and innovations in the use of these materials for enhanced performance and efficiency.

2. Experimental Methods

The main objective of this study is to characterize the effects of poro-elasticity on the deformation and flow rate through thin highly compliant membranes. To this end, membranes of different material strengths and different rates of porosity are fabricated and characterized on a bulge test

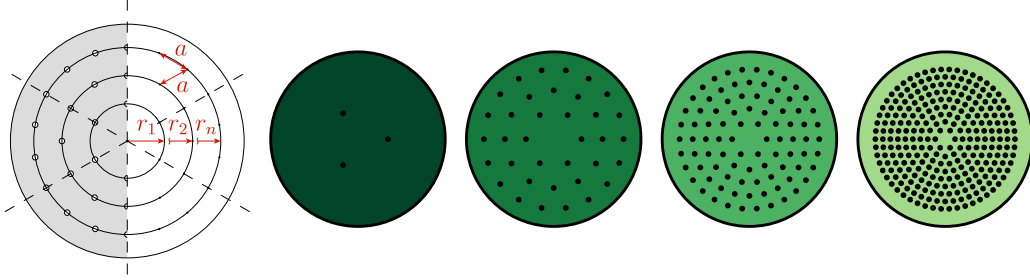


Figure 1: Porosity definition for the radial six-spoke pattern and examples of patterns with 1, 3, 5, and 9 layers of pores leading to initial solidities of $\epsilon_0 = 0.9987, 0.985, 0.962,$ and 0.886 . A radial three-spoke pattern is used for the $m = 1$ layer porosity membranes and six-spoke patterns for membranes with $m = 3, 5$ and 9 layers.

pressure chamber. In the following sections, we outline the different porosity patterns employed, the membrane fabrication process, and introduce the experimental test stand with all its components.

2.1. Poro-elastic membranes

The membranes in this study were created using a platinum-based addition-cure silicone rubber (*Dragon Skin FX Pro, Shore Hardness 2A; Smooth-On Inc., Macungie, PA*). This silicone rubber is created by mixing together three components: Part A, which is a silicone hydride, Part B, a vinyl compound that functions as a catalyst for the polymerization, and a thinning agent (*TC 5005-C; BJB Enterprises Inc., Tustin, CA*) which changes the material stiffness of the cured membranes. Membranes with three different portions of thinner (5%, 25%, and 45%) were fabricated, corresponding to shear moduli of $G = [32.04 \text{ kPa}, 13.22 \text{ kPa}, 6.53 \text{ kPa}]$, and locking parameters of $J_m = [28.97, 36.47, 47.52]$. The membranes are then cast onto level plates and their thickness is controlled with a mechanical micrometer film applicator. After the membranes are cured the thickness of each membrane is measured with an outside micrometer. The average thickness and standard deviation of all membranes used in this study was $h = 125 \pm 5 \text{ }\mu\text{m}$.

The porosity is implemented by cutting a symmetric pattern onto the membrane sheets with a laser cutter, and the size of the pores ($d = 0.61 \text{ mm}$) measured with the stereo camera setup (Figure 2b). The patterns are based on a 6-spoke pattern, a radial expanding pattern commonly used in many mathematical and technical applications (Figure 1). Starting at an initial radius r_1 six pores are distributed evenly on a circle ($\Delta\phi = 60^\circ$). Then, a

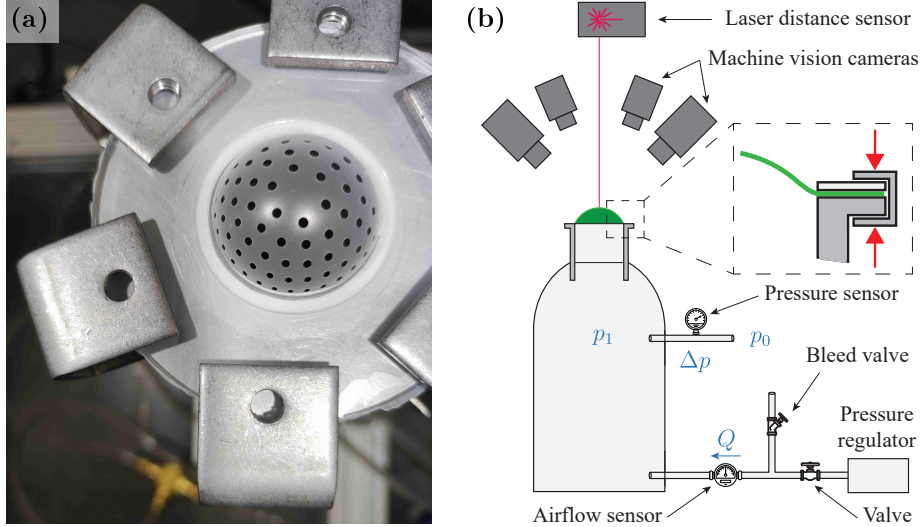


Figure 2: a. Top view on the experimental apparatus showing expanding pores for a five-layer pore pattern. b. Bulge test stand with direct measurements of pressure difference Δp , flow rate Q , and sample height w_0 . Machine vision cameras in stereo configuration track the shape and local stretch of the samples.

second layer at a radius r_2 is chosen. Pores are distributed on the same initial six angles ϕ , but in addition six additional pores are placed one between each spoke. On the third layer, the process is repeated but instead two additional pores are equidistantly placed between each spoke. The pattern is continued until the final m -th layer at radius r_m . No pore is placed at the center of the membrane. The number of all pores can thus be calculated with $n = \sum_1^m 6(m-1)$ for the different patterns. The radii of each layer are chosen such that the difference between the minimal distance between two pores on a layer and the distance between pores of adjacent layers for non-spoke pores is minimal ($\approx \text{const.}$) (Figure 1). The initial radius for each layer is chosen relative to the diameter of the membrane D at $r_m = 0.80(D/2)$ for every pattern and expanded inwards until r_1 . Note that the only exception to this pattern is the membrane with only one layer and which has three pores at $r_1 = r_m = 0.34(D/2)$. A total of 15 membranes were manufactured and tested varying over three different material parameters (G and J_m), and five different porosity patterns including one non-porous membrane for reference.

2.2. Pressure chamber

To characterize the material behavior of the poro-elastic membranes different membrane samples are being subjected to increasing pressure loading on a bulge test stand (Figure 2b). The pressure chamber consists of a large tank (≈ 1.5 L) to ensure that the flow velocities inside the chamber are negligible and the tank acts as a reservoir of infinite size. On top of the tank a circular pipe with a flat flange is connected to provide an interface for the different membrane samples to be tested. The interface opening and effective diameter of the membrane samples is $D = 0.03$ m (Figure 3a). The samples are mounted on an acrylic ring and fixed in place with a thin plastic sheet. The acrylic ring with the sample is then mounted and sealed on the pressure chamber interface (Figure 2b, inset). The tank is supplied with a constant flow rate Q at a pressure p_1 from an external pressure supply and regulated by a mechanical valve. In addition to the main valve, a bleed valve is installed to avoid pressure build-up in the chamber for non-porous and solidity samples.

The pressure difference Δp between the interior p_1 and exterior p_0 is measured with a differential pressure transducer (*Setra 26512R5WD2BT1F*, *Setra Systems Inc, Boxborough, Massachusetts*) located near the membrane, in the upper part of the tank. The flow rate Q passing through the porous membranes is measured through the supply flow rate at the bottom the tank using a digital air flow sensor (*Honeywell Zephyr, HAFUHT0100L4AXT*, *Honeywell International Inc., Charlotte, NC*) rated up to $Q = 1.67 \times 10^{-3}$ m³/s (= 100 SLPM). The deformation of the center of the membrane samples is measured with a laser distance sensor (*AR700-16 Acuity Laser Sensor, AP7420160, Schmitt Measurement Systems, Portland, OR*) positioned above the membrane (Figure 2b). Four machine vision cameras (*Alvium 1800 U-500m, Allied Vision, Stadtroda, Germany*) are positioned with equal spacing at 45° inclination with respect to the center-line of the membranes to track the position of the pores and additional tracking markers on the samples. The stereo camera tracking allows to reconstruct the full 3D shape of the porous membranes including the local stress and strain at each position on the membrane. All measurements devices are synchronized and data is recorded over 5 seconds after waiting 30 seconds for the pressure to equilibrate. The recorded signals are then averaged in time for further processing and analysis. One set of stereo images is taken at each pressure level Δp . The entire system is considered as stationary as no discernible time-variance of Δp , Q , or w_0 is observed for a fixed measurement point where Δp is regulated by the valve

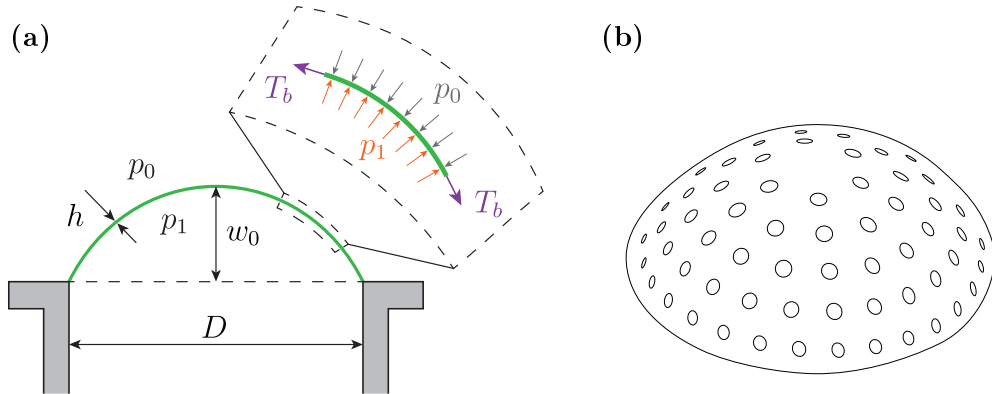


Figure 3: a. Dimensions of the expanding membrane and the relation between the internal and external pressure with the membrane tension, b. Schematic of expanding pores for a five-layer porosity pattern.

position.

3. Results and Discussion

In this study, we characterize the behavior of poro-elastic membranes under various pressure loadings and establish scaling laws relevant to the design of poro-elastic engineering applications. We begin by analyzing the deformation of the membranes in response to applied pressure, followed by an examination of the relationship between membrane deformation and through-flow.

3.1. Elastic characterization and modeling

Initially, the membranes are flat disks with a diameter D and a pre-stretch λ_0 , applied during mounting. The pre-stretch, ranging from 1% to 10%, is measured individually before each experiment.

When the pressure difference (Δp) between the inner chamber and the ambient pressure increases, the membranes bulge outward, forming a spherical cap with a maximum height (w_0) at the center for both porous and non-porous membranes (Figure 3a). This spherical cap deformation has been previously demonstrated by Das et al. (2020) and is also observed in our experiments with porous membranes.

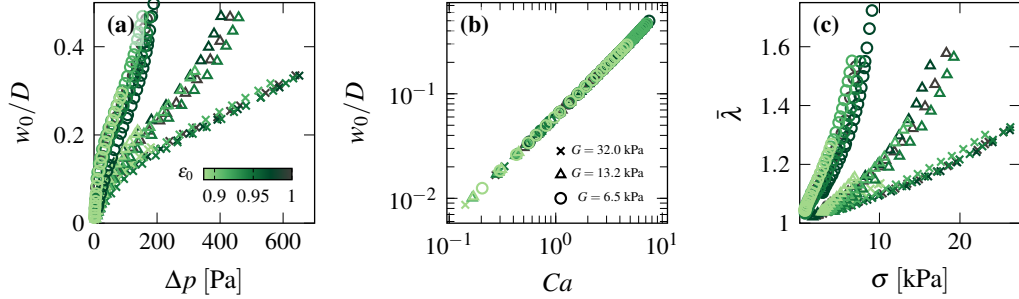


Figure 4: (a) Normalized membrane center-line deformation w_0/D as a function of the pressure difference Δp acting on the membrane, (b) Normalized membrane center-line deformation as a function of the Cauchy number Ca , and (c) Average membrane stretch $\bar{\lambda}$ as a function of membrane stress σ , shown for different solidities ϵ_0 and materials G .

To develop a general expression for the membrane-average stress (σ) and stretch ($\bar{\lambda}$), we measure the center-line deformation (w_0) and pressure difference (Δp) across a range of material properties and porosity patterns (Figure 4a). Note that bars on top of variables, $(\bar{\quad})$, indicate membrane-average quantities, where in further analysis local stretch analysis $\lambda(r, \sigma)$ will be presented in Section 3.2.

The center-line deformation reaches up to $w_0/D = 0.5$ for the most compliant membranes. The applied pressure varies from $\Delta p = 0$ to 650 Pa. The membrane deformation groups by stiffness, indicated by different markers, with porosity having minimal impact on the deformation variation, indicated by the different colors. The silicone-based elastomers exhibit hyper-elastic behavior under pressure loading, consistent with the findings of Das et al. (2020). Hyper-elastic materials can sustain large strains before strain-stiffening occurs, as seen in the inflection points for intermediate and highly flexible membranes (Figure 4a).

The biaxial stress–strain relationship of the hyperelastic membranes is well described by a two-parameter Gent model (Das et al., 2020):

$$\sigma = G_m \left(\lambda - \frac{1}{\lambda^2} \right), \quad (1)$$

where the effective shear modulus is given by

$$G_m = \frac{GJ_m}{J_m - I_1 + 3}. \quad (2)$$

Here, G is the shear modulus, and J_m is the locking parameter, which characterize the Neo-Hookean response of the material, and I_1 is the first invariant of the deformation tensor. The material parameters can be determined either from uniaxial tensile tests or directly from bulge test measurements in our experiments.

Local deformation analysis (Section 3.2) confirms that the biaxial stress–strain relationship provides a good approximation of the overall membrane deformation. However, its accuracy diminishes for large deformations ($w_0 \rightarrow 0.5D$) and near the membrane mount ($r_0 \rightarrow 0.5D$), where additional effects may become significant.

Having access to the stress and stretch allows also to calculate the tension (T_b) in the membranes from the first Piola-Kirchhoff stress according to Das et al. (2020):

$$T_b = G_m h \left(1 - \frac{1}{\lambda^6} \right). \quad (3)$$

We introduce a Cauchy number as the ratio of membrane tension to pressure loading:

$$Ca = \frac{\Delta p D}{T_b}. \quad (4)$$

The Cauchy number correlates well with the membrane’s center-line deformation (Figure 4b), and the data collapses on one line with a power law dependence. Importantly, for these relatively low levels of porosity (solidity ranges from $\epsilon_0 = 0.886$ to 0.9987) the porosity does not have a discernible effect on the structural response of the membrane, as its relation with any applied stress is consistent between patterns. This scaling relationship allows us to normalize and predict membrane deformation as a function of pressure if the material properties are known or determined via the bulge tests as done in this study. Furthermore, these predictions can be applied to systems where pressure is applied by fluid dynamic loading ($q = 0.5\rho U^2$), such as in wind tunnel experiments (Mathai et al., 2023).

The elastic scaling model allows us to compare internal membrane stress relative to stretch (Figure 4c). Note that the stretch λ includes a pre-stretch λ_0 determined under zero pressure conditions at the beginning of the experiments. The non-linear behavior observed in the stress-stretch curves is well captured by the model, displaying consistent curvature for each of the three different materials which agrees well with other studies on hyper-elastic membranes (Sasso et al., 2008; Das et al., 2020).

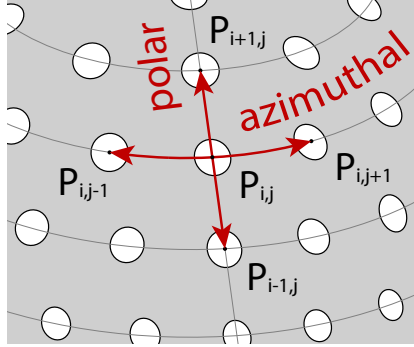


Figure 5: Local stretch $\lambda_{i,j}$ definition for each radial position of pores.

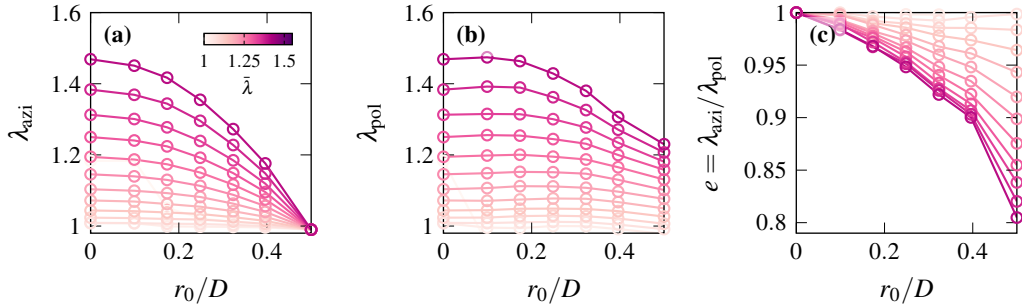


Figure 6: (a) Azimuthal stretch (λ_{azi}), (b) Polar stretch (λ_{pol}), and (c) Stretch eccentricity ($e = \lambda_{azi}/\lambda_{pol}$) as a function of initial radial position (r_0), for different radial-average stretches ($\bar{\lambda}$). The local stretch is shown for a five-layer pattern and low stiffness ($G = 6.5$ kPa), but is representative for all tested membranes.

3.2. Local membrane stretch

In order to understand the flow through the porous membrane, we need to first determine the geometry of the evolving pore distribution of the expanding membranes. We measure the pore positions using the pores itself as tracers, and applying markers to membranes without or only very few pores. The open area of the pores is estimated by relating the membrane-average stretch ($\bar{\lambda}$) to the local stretch of the pores across the membrane. The positions of all pores are tracked optically (Figure 2b) to determine the local stretch $\lambda(r, \bar{\lambda})$ for each pore based on its radial position and the overall deformation of the membrane. The azimuthal and polar stretches are calculated on the spherical cap membrane shape using the relative positions of the pores (Figure 5). The azimuthal stretch (λ_{azi}) is determined by the

relative distance along the membrane surface between two adjacent pores at the same radial position, while the polar stretch (λ_{pol}) is determined by the relative radial distance between pores at adjacent radial positions:

$$\lambda_{\text{azi}}(r, \lambda) = l_{\text{azi}}(r, \lambda) - l_{\text{azi},0}(r) \quad \text{and} \quad \lambda_{\text{pol}}(r, \lambda) = l_{\text{pol}}(r, \lambda) - l_{\text{pol},0}(r), \quad (5)$$

with the central differences $l_{\text{azi}}(\lambda) = 0.5 \overline{P_{i,j-1}P_{i,j+1}}$ and $l_{\text{pol}}(\lambda) = 0.5 \overline{P_{i-1,j}P_{i+1,j}}$ (Figure 5).

Due to the symmetry of the pore pattern, the local stretch remains constant between different pores at the same radial position (r). The azimuthal stretch increases across all radial positions with increasing deformation, except at the position closest the membrane edge (Figure 6a), where the membrane is clamped and cannot expand azimuthally. Here, the azimuthal stretch remains at the pre-stretch value λ_0 . With higher average stretch (λ), the azimuthal stretch (λ_{azi}) is greater at the center compared to the outer parts of the membrane where the membrane is geometrically restricted from expanding. The radial stretch evolution could also be observed on hyper-elastic materials tested on a bulge setup by Sasso et al. (2008), although its implications for their study are not further discussed. The polar stretch (λ_{pol}) initially stretches uniformly across the membrane (Figure 6b) but shows higher stretch near the membrane's center at higher deformations as well.

The difference between azimuthal and polar stretches results in a stretch eccentricity (e), which varies with the pores' initial radial position (r_0) and membranes overall deformation given by $\bar{\lambda}$. Near the membrane's center, the pores remain circular, if we assume that the pores stretch at the same rate as the membrane. Towards the outer regions, the stretch becomes more eccentric with increased $\bar{\lambda}$ due to restricted azimuthal stretch at the mounting radius ($r_0 = 0.5D$). The eccentricity reaches up to $e = 0.8$ for the highest deformation presented ($\bar{\lambda} = 1.5$). These results indicate that the assumption of biaxial stress-strain holds across most of the membrane, except at the highest stretches and near the membrane mount.

From the local stretch analysis, we can directly determine the pore size evolution as a function of the membrane-average stretch ($\bar{\lambda}$) and the radial position (r) of the pores (Figure 7a). At small and initial $\bar{\lambda}$, the pore diameter (d) remain uniform across the membrane's radial position (r_0/D) and are approximately $d \approx d_0$. As the membrane stretch increases, pores near the center ($r_0 = 0.1D$) expand up to $d = 1.5d_0$. A gradient of decreasing pore size evolves from the inner region of the membrane to the outer edge,

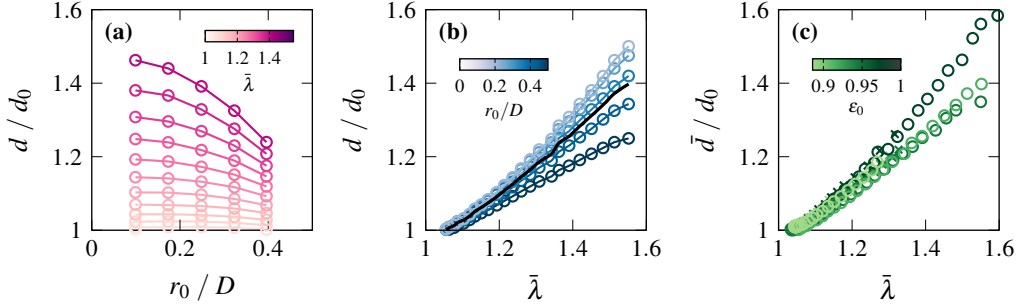


Figure 7: (a) Local pore diameter (d/d_0) as a function of the initial radial position (r_0/D) for various membrane stretches ($\bar{\lambda}$). (b) Local pore diameter as a function of the membrane stretch, the different colors correspond to the initial radial position. The black line represents the membrane average diameter \bar{d} across the membrane. (c) Membrane average pore diameter (\bar{d}/d_0) as a function of the membrane stretch, the different colors correspond to the initial solidity (ϵ_0). The local diameters in a and b are shown for a five-layer pattern and low stiffness ($G = 6.5$ kPa) membrane, but are qualitatively representative for all tested membranes.

corresponding to the radial stretch distributions observed in Figure 6. This gradient becomes more pronounced with increasing membrane deformation ($\bar{\lambda}$). At the maximum observed membrane stretch ($\bar{\lambda} = 1.6$), the pore size difference between the innermost and outermost regions exceeds 20%.

To quantify the pore size evolution across the membrane, we calculate the pore-average diameter (\bar{d}) according to the pore-average area (\bar{a}):

$$\bar{d} = 2\sqrt{\sum^n \frac{a(r)}{\pi n}} \quad (6)$$

We use this parameter to characterize the pore size evolution over the entire membrane and will relate it to the flow rate through the porous membranes in subsequent sections. We observe that the membrane-average pore diameter (\bar{d}) falls approximately midway between the minimum and maximum local pore diameters (Figure 7b). Interestingly, despite the number of pores increasing by six per layer, the open area summed for each pore layer remains roughly constant.

The membrane-average pore diameter (\bar{d}) and the local diameters at radii $r_0 > 0.3D$ increase linearly or sub-linearly with increasing \bar{d} , whereas pores at radii closer to the membrane center ($r_0 < 0.3D$) exhibit super-linear growth.

Comparing different pore patterns, we find that the membrane-average

pore diameter collapses onto a single trend, except for the minimal pore pattern (dark green), which shows a distinct slope at higher $\bar{\lambda}$ (Figure 7c). In the following section, we use \bar{d} to characterize the membrane flow rate Q and define a Reynolds number for flow through the pores.

We summarize the key findings that emerge from the local stretch analysis: First, local stretch is higher towards the membrane center compared to the outer radii, leading to larger pore diameters and open areas near the center. At larger global deformations, the pore stretch becomes increasingly eccentric at the outer radii due to azimuthal and polar stretch differences. Second, the pore diameter scales directly with local stretch. The membrane-average diameter shows consistent scaling behavior between different porosity patterns, with a linear to quadratic dependence on $\bar{\lambda}$. In the following analysis, we consider the increase in pore area to accurately predict flow rates through the porous membranes.

3.3. Flow rate scaling

We now examine the relationship between the measured flow rate (Q) through the membrane's pores and the pressure loading (Δp). The flow rate reaches up to $Q = 1.62 \times 10^{-3} \text{ m}^3/\text{s}$ at the highest pressures ($\Delta p \approx 650 \text{ Pa}$) for membranes with intermediate stiffness and initial solidity (Figure 8a). Softer membranes achieve maximum flow rates at lower pressures, while stiffer membranes with low initial porosity are limited to low flow rates before reaching the limit of the pressure sensor or the maximum considered expansion of the membrane ($w_0 = 0.5D$). Since the membrane-average stretch ($\bar{\lambda}$) is also a function of the pressure (Δp), the same flow rate (Q) can correspond to different porous geometries, or different flow rates can be observed for the same geometry.

Understanding the flow rate in relation to the membrane's shear modulus and pressure loading requires consideration of two factors: the pressure differential (Δp), which drives the flow, and the expanded solidity $\epsilon(\bar{\lambda})$, which governs area available for flow through the membrane.

A discharge coefficient (C_d) accounts for pressure losses due to an orifice geometry and is defined as the ratio of the measured flow rate to the ideal flow rate through an infinitely large opening (Merritt, 1967; Miller, 1996):

$$C_{d,\text{single}} = \frac{Q_{\text{exp}}}{Q_{\text{ideal}}} = \frac{Q}{a\sqrt{\frac{2\Delta p}{\rho}}}, \quad (7)$$

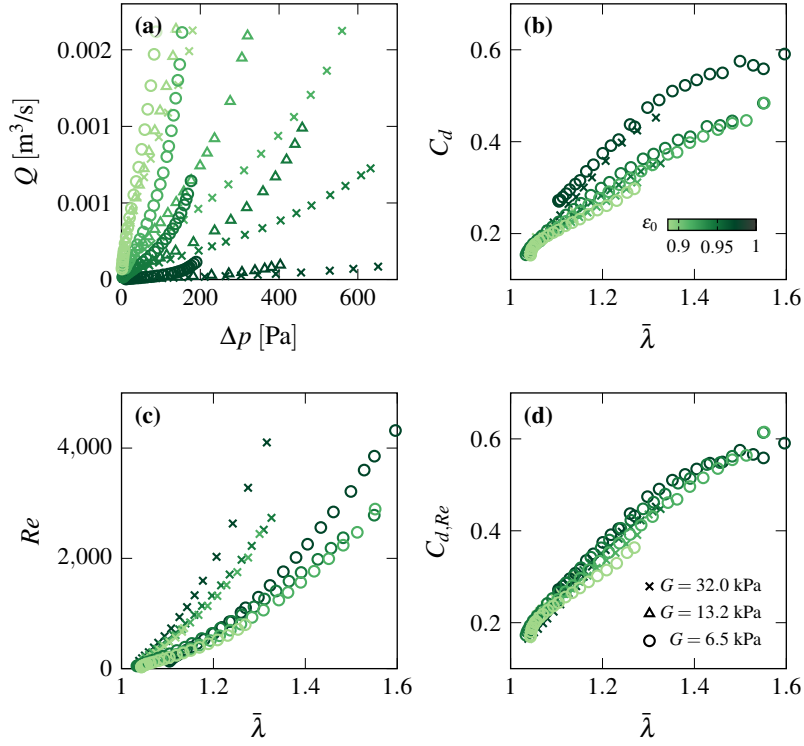


Figure 8: (a) Volume flow rate Q as a function of the pressure difference Δp , (b) Discharge coefficient C_d as a function of the membrane-average stretch $\bar{\lambda}$, (c) Reynolds number Re as a function of $\bar{\lambda}$, (d) Reynolds number scaled discharge coefficient $C_{d,Re}$ as a function of $\bar{\lambda}$. All plots shown for different solidities (ϵ - color gradient) and material stiffnesses (G - markers) as indicated in the legends.

where a is the orifice or pore area and ρ is the density of the fluid.

Treating the porous membranes as a series of non-interacting, parallel orifice flows, we define a membrane-averaged discharge coefficient for the system:

$$C_d = \frac{Q}{n\bar{a}\sqrt{\frac{2\Delta p}{\rho}}}, \quad (8)$$

where n is the number of pores of the pattern (Figure 1), and \bar{a} the membrane-average pore area. Here, the pore area expansion is measured from the local stretch of the pores at different pressures, and an average, representative pore area calculated (see Section 3.2).

The discharge coefficient (C_d) scales the measured flow rate (Q) relative to the membrane-average stretch ratio ($\bar{\lambda}$) (Figure 8b) and accounts for both the pressure difference and changes in the pore diameter due to the membrane stretch. The coefficient increases with higher stretch ratios due to increased pore sizes which leads to lower pressure losses. A discharge coefficient of $C_d \approx 0.6$ is reached for the highest solidity (ϵ_0) membranes which is a typical value reached for single orifices or orifices at low to intermediate pore Reynolds numbers (Merritt, 1967; Huang et al., 2013). Here, the flow rate scaling with the discharge coefficient splits the data into two distinct groups (Figure 8b), where in particular the three-hole pattern with the highest initial solidity has a different slope compared to membranes with lower solidity.

The deviation of the discharge coefficient suggest a change in the flow characteristics for the minimal pattern of only three holes and initial solidity of $\epsilon_0 = 0.9987$ (Figure 1) compared to the others. The minimal pattern will have much lower flow rates at the same membrane stretch or will have much higher pressure gradients to reach the same flow rate (Figure 8a).

We can identify the following parameter to impact the discharge coefficient for perforated disks from a dimensional analysis:

- Fluid velocity through the pores (u)
- Fluid density (ρ)
- Dynamic viscosity of the fluid (μ)
- Pore diameter (d)
- Pipe/Disk area (A)
- Number of pores (n)

Note that the thickness of the disk (h) or a pitch angle (θ) of the plate

can be additional parameters that influence the discharge coefficient, which in our study are considered constant (Kolodzie and Van Winkle, 1957).

To investigate the influence of viscous versus inertial effects, we can define a Reynolds number (Re) for the flow through the pores with the representative pore diameter (\bar{d}) averaged across all pores. The pore diameter can be expressed with the pore area ($\bar{d} = 2\sqrt{\bar{a}/\pi}$), and the flow velocity through the pores ($u = Q/(n\bar{a})$). The through-flow Reynolds number becomes now:

$$Re = \frac{2\rho Q}{\mu\sqrt{\pi n\bar{a}}} \quad (9)$$

In this study, the Reynolds number ranges from $Re = 30$ to 4500 depending on the tested membrane stiffness and porosity pattern (Figure 8c). This wide range of Reynolds number magnitudes and the associated ratio between viscous and inertial contributions to the discharge coefficient makes the prediction of pressure losses inherently complex and non-linear (Merritt, 1967). For a constant flow rate (Q) and stretch (λ), the flow velocity (u) through the pores will vary greatly with the porous pattern and material properties. For softer membranes or membranes with lower solidity (ϵ_0), the Reynolds numbers grows slower as a function of $\bar{\lambda}$. The membranes deform at lower pressure and there is a larger open pore area which leads to lower velocities and in consequence lower Reynolds numbers. The opposite is observed for stiffer and less porous membranes. For the same porous pattern, the Reynolds number can double between membranes of different stiffness.

For $Re < 10^4$, the discharge coefficient is influenced by variations in flow rate, velocity, shape factor, and viscosity (Merritt, 1967; Miller, 1996). Consequently, all the measurements presented must account for a significant Reynolds number effect on the discharge coefficient, which may explain the differences in C_d scaling observed earlier in Figure 8b.

We investigate the Reynolds number dependency of the porous membranes by defining a Reynold's dependent discharge coefficient:

$$C_{d,Re} = Re^\alpha C_d \quad (10)$$

where the parameter α controls the dependency on the Reynolds number.

We can then expand Equation (10) to include the measured flow parameters of the problem. We sort the terms between Reynolds independent and case constant values, which leaves only the ratio between the measured flow

rate and the pore area to control the variance in the discharge coefficient:

$$C_{d,Re} = \frac{2^{\alpha-0.5} \rho^{\alpha+0.5}}{\underbrace{\pi^{0.5\alpha} \mu^\alpha \Delta p^{0.5}}_{\text{case or Reynolds number independent}}} \frac{Q^{\alpha+1}}{n^{0.5\alpha} \bar{a}^{0.5\alpha+1}} \quad (11)$$

The left fraction of Equation (11) varies with the pressure difference Δp at the same for each membrane stiffness or pore pattern. This leaves the fraction between measured flow rate (Q) and average pore area (\bar{a}) to be impacted by the scaling factor α .

When we vary the Reynolds number scaling parameter α , we find that for $\alpha = 0.03$ the data for all our cases collapses onto one slope (Figure 8d). This shows that the Reynolds number plays an important role in predicting the discharge coefficient for the presented range of intermediate Reynolds numbers ($Re < 5000$) across the different patterns.

Overall, the discharge coefficient increases with Reynolds number, consistent with the reduction in viscous pressure losses at higher Re . The poro-elastic system presented here involves several coupled material and flow parameters that respond to an increase in pressure difference. As the membrane stretches, the pores expand, leading to a pressure drop that depends on both the collective behavior of all pores and the pore-scale Reynolds number. Eventually, the discharge coefficient is expected to level out at higher Reynolds numbers ($Re > 10^4$) (Merritt, 1967; Huang et al., 2013) which are not covered in this study, but the trend in Figure 8d towards the higher Re suggests.

4. Conclusion

This study provides a comprehensive analysis of the impact of poro-elastic properties on the deformation and flow rate through thin compliant membranes. Prior research has largely focused on theoretical and numerical studies, with limited experimental data available. Our work expands on these foundations by experimentally investigating the deformation and flow rate behavior of silicone rubber membranes with varying material stiffness and porosity patterns.

We fabricated membranes with different porosity levels, ranging from solid to highly porous structures, and subjected them to controlled pressure loading. The membranes were tested using a bulge test setup, allowing us

to measure deformation, pore flow rate, and local stresses and strains of the membranes. Our findings show that the porosity does not affect the deformation characteristics of the membranes as a function of the pressure loading. This allows us to apply an elastic scaling model developed for solid hyper-elastic polymers. The experimental data agrees well with the two-parameter Gent model for a wide range of pressure loading conditions.

The pressure-driven flow rate through the open pores is influenced by two independent membrane parameters - the material stiffness and the porosity. We perform a three-dimensional reconstruction of the porous membrane from stereo photogrammetry measurements and determine the local stretch of the membrane around each pore. We find that the stretch increases towards the center of the membrane and is reduced towards the outer parts of the membrane, especially in azimuthal stretch direction. As a result, the pores at the center of the membrane grow at a relatively higher rate when the membrane stretches. We find that the combined area of all pores within a layer is approximately constant across the membrane, which makes an membrane-average pore size diameter a good characteristic length scale of the porous pattern. The membrane-average pore diameter scales with the same linear to quadratic rate across most porous patterns apart from the minimal porous pattern. This allows us to predict the effective porosity as a function of the membrane stretch or pressure for poro-elastic membranes.

In the final part of the analysis, we introduce a discharge coefficient that scales the experimentally measured flow rate to the ideal flow rate through the open pore area. We incorporate the deformation and pore expansion scaling from our previous analysis to determine a discharge coefficient for each porous pattern at each membrane stretch. While this scaling works across various porosities and material parameters, it diverges for membranes with high stiffness and low porosity. In these cases, the local pore velocity and Reynolds number increase significantly compared to cases with higher porosity. We define a Reynolds number correction term for the discharge coefficient which incorporates the local pore size and velocity and find consistent prediction of the new discharge coefficient across all our measurements.

Overall, this study advances the understanding of poro-elastic membrane behavior, providing valuable insights for the design of engineering applications involving flexible and porous structures. The experimental framework and scaling laws developed in this work can be used to predict membrane performance in various practical scenarios, including fluid-structure interaction systems and bio-inspired aerodynamic designs. Our findings pave the

way for future research on the role of porosity and material properties in the aeroelastic performance of compliant structures. Especially, the ability to modulate the discharge coefficient as a function of pressure loading and material properties make this type of system interesting for adaptive designs.

CRedit authorship contribution statement

Alexander Gehrke: Writing – original draft, Methodology, Investigation, Conceptualization, Formal analysis. **Zoe King:** Resources, Investigation. **Kenneth S. Breuer:** Writing – review & editing, Supervision, Conceptualization, Funding acquisition.

Declaration of competing interest

The authors declare that they have no known competing financial interests or personal relationships that could have appeared to influence the work reported in this paper.

Acknowledgments

This work was financially supported by the United States National Science Foundation (NSF) grant GR5260547.

Data availability

Data will be made available on request.

References

- Aldheeb, M., Asrar, W., Sulaeman, E., Omar, A.A., 2018. Aerodynamics of porous airfoils and wings. *Acta Mechanica* 229, 3915–3933. URL: <http://link.springer.com/10.1007/s00707-018-2203-6>, doi:10.1007/s00707-018-2203-6. number: 9.
- Baddoo, P.J., Hajian, R., Jaworski, J.W., 2021. Unsteady aerodynamics of porous aerofoils. *Journal of Fluid Mechanics* 913, A16. URL: https://www.cambridge.org/core/product/identifier/S0022112020010319/type/journal_article, doi:10.1017/jfm.2020.1031.

- Brunet, Y., 2020. Turbulent Flow in Plant Canopies: Historical Perspective and Overview. *Boundary-Layer Meteorology* 177, 315–364. URL: <https://link.springer.com/10.1007/s10546-020-00560-7>, doi:10.1007/s10546-020-00560-7. number: 2-3.
- Castro, I.P., 1971. Wake characteristics of two-dimensional perforated plates normal to an air-stream. *Journal of Fluid Mechanics* 46, 599–609. URL: https://www.cambridge.org/core/product/identifier/S0022112071000727/type/journal_article, doi:10.1017/S0022112071000727. number: 3.
- Cummins, C., Seale, M., Macente, A., Certini, D., Mastropaolo, E., Viola, I.M., Nakayama, N., 2018. A separated vortex ring underlies the flight of the dandelion. *Nature* 562, 414–418. URL: <http://www.nature.com/articles/s41586-018-0604-2>, doi:10.1038/s41586-018-0604-2. number: 7727.
- Cummins, C., Viola, I.M., Mastropaolo, E., Nakayama, N., 2017. The effect of permeability on the flow past permeable disks at low Reynolds numbers. *Physics of Fluids* 29, 097103. URL: <https://pubs.aip.org/pof/article/29/9/097103/967688/The-effect-of-permeability-on-the-flow-past>, doi:10.1063/1.5001342. number: 9.
- Das, A., Breuer, K.S., Mathai, V., 2020. Nonlinear modeling and characterization of ultrasoft silicone elastomers. *Applied Physics Letters* 116, 203702. URL: <http://aip.scitation.org/doi/10.1063/5.0006791>, doi:10.1063/5.0006791. number: 20.
- Detournay, E., 1993. *Comprehensive rock engineering: principles, practice and projects. Fundamentals of poroelasticity 2*, 113–171. Publisher: Pergamon Press.
- Dowell, E.H., Hall, K.C., 2001. Modeling of Fluid-Structure Interaction. *Annual Review of Fluid Mechanics* 33, 445–490. URL: <https://www.annualreviews.org/content/journals/10.1146/annurev.fluid.33.1.445>, doi:<https://doi.org/10.1146/annurev.fluid.33.1.445>. number: Volume 33, 2001 Publisher: Annual Reviews Type: Journal Article.

- Eberle, A.L., Reinhall, P.G., Daniel, T.L., 2014. Fluid–structure interaction in compliant insect wings. *Bioinspiration & Biomimetics* 9, 025005. URL: <https://iopscience.iop.org/article/10.1088/1748-3182/9/2/025005>, doi:10.1088/1748-3182/9/2/025005. number: 2.
- Ehret, A.E., Bircher, K., Stracuzzi, A., Marina, V., Zündel, M., Mazza, E., 2017. Inverse poroelasticity as a fundamental mechanism in biomechanics and mechanobiology. *Nature Communications* 8, 1002. URL: <https://www.nature.com/articles/s41467-017-00801-3>, doi:10.1038/s41467-017-00801-3. number: 1.
- Gehrke, A., Mulleners, K., 2025. Highly deformable flapping membrane wings suppress the leading edge vortex in hover to perform better. *Proceedings of the National Academy of Sciences* 122, e2410833121. URL: <https://pnas.org/doi/10.1073/pnas.2410833121>, doi:10.1073/pnas.2410833121.
- Gehrke, A., Richeux, J., Uksul, E., Mulleners, K., 2022. Aeroelastic characterisation of a bio-inspired flapping membrane wing. *Bioinspiration & Biomimetics* 17, 065004. URL: <https://iopscience.iop.org/article/10.1088/1748-3190/ac8632>, doi:10.1088/1748-3190/ac8632. number: 6.
- Geyer, T., Sarradj, E., Fritzsche, C., 2010. Measurement of the noise generation at the trailing edge of porous airfoils. *Experiments in Fluids* 48, 291–308. URL: <http://link.springer.com/10.1007/s00348-009-0739-x>, doi:10.1007/s00348-009-0739-x. number: 2.
- Heinrich, H.G., Haak, E.L., 1971. Stability and drag of parachutes with varying effective porosity. Technical Report. Minnesota University, Minneapolis.
- Huang, S., Ma, T., Wang, D., Lin, Z., 2013. Study on discharge coefficient of perforated orifices as a new kind of flowmeter. *Experimental Thermal and Fluid Science* 46, 74–83. URL: <https://linkinghub.elsevier.com/retrieve/pii/S0894177712003317>, doi:10.1016/j.expthermflusci.2012.11.022.
- Iosilevskii, G., 2011. Aerodynamics of permeable membrane wings. *European Journal of Mechanics - B/Fluids* 30, 534–542. URL: <https://>

- linkinghub.elsevier.com/retrieve/pii/S0997754611000458, doi:10.1016/j.euromechflu.2011.05.003. number: 5.
- Iosilevskii, G., 2013. Aerodynamics of permeable membrane wings. Part 2: Seepage drag. *European Journal of Mechanics - B/Fluids* 39, 32–41. URL: <https://linkinghub.elsevier.com/retrieve/pii/S0997754612001367>, doi:10.1016/j.euromechflu.2012.11.004.
- Jaworski, J.W., Peake, N., 2013. Aerodynamic noise from a poroelastic edge with implications for the silent flight of owls. *Journal of Fluid Mechanics* 723, 456–479. URL: https://www.cambridge.org/core/product/identifier/S0022112013001390/type/journal_article, doi:10.1017/jfm.2013.139.
- Jaworski, J.W., Peake, N., 2020. Aeroacoustics of Silent Owl Flight. *Annual Review of Fluid Mechanics* 52, 395–420. URL: <https://www.annualreviews.org/doi/10.1146/annurev-fluid-010518-040436>, doi:10.1146/annurev-fluid-010518-040436. number: 1.
- Jiang, Y., Zhao, P., Cai, X., Rong, J., Dong, Z., Chen, H., Wu, P., Hu, H., Jin, X., Zhang, D., Liu, H., 2022. Bristled-wing design of materials, microstructures, and aerodynamics enables flapping flight in tiny wasps. *iScience* 25, 103692. URL: <https://linkinghub.elsevier.com/retrieve/pii/S258900422101662X>, doi:10.1016/j.isci.2021.103692. number: 1.
- Jones, T.J., Jambon-Puillet, E., Marthelot, J., Brun, P.T., 2021. Bubble casting soft robotics. *Nature* 599, 229–233. URL: <https://www.nature.com/articles/s41586-021-04029-6>, doi:10.1038/s41586-021-04029-6. number: 7884.
- Kanai, T., Takizawa, K., Tezduyar, T.E., Tanaka, T., Hartmann, A., 2019. Compressible-flow geometric-porosity modeling and spacecraft parachute computation with isogeometric discretization. *Computational Mechanics* 63, 301–321. URL: <http://link.springer.com/10.1007/s00466-018-1595-4>, doi:10.1007/s00466-018-1595-4. number: 2.
- Kim, Y., Peskin, C.S., 2006. 2-D Parachute Simulation by the Immersed Boundary Method. *SIAM Journal on Scientific Computing* 28, 2294–2312. URL: <http://epubs.siam.org/doi/10.1137/S1064827501389060>, doi:10.1137/S1064827501389060. number: 6.

- Kolodzie, P.A., Van Winkle, M., 1957. Discharge coefficients through perforated plates. *AICHE Journal* 3, 305–312. URL: <https://aiche.onlinelibrary.wiley.com/doi/10.1002/aic.690030304>, doi:10.1002/aic.690030304.
- Kolomenskiy, D., Farisenkov, S., Engels, T., Lapina, N., Petrov, P., Lehmann, F.O., Onishi, R., Liu, H., Polilov, A., 2020. Aerodynamic performance of a bristled wing of a very small insect: Dynamically scaled model experiments and computational fluid dynamics simulations using a revolving wing model. *Experiments in Fluids* 61, 194. URL: <https://link.springer.com/10.1007/s00348-020-03027-0>, doi:10.1007/s00348-020-03027-0. number: 9.
- Koo, J.K., James, D.F., 1973. Fluid flow around and through a screen. *Journal of Fluid Mechanics* 60, 513. URL: http://www.journals.cambridge.org/abstract_S0022112073000327, doi:10.1017/S0022112073000327. number: 03.
- Malandrino, A., Moeendarbary, E., 2019. Poroelasticity of Living Tissues, in: *Encyclopedia of Biomedical Engineering*. Elsevier, pp. 238–245. URL: <https://linkinghub.elsevier.com/retrieve/pii/B978012801238399932X>, doi:10.1016/B978-0-12-801238-3.99932-X.
- Mathai, V., Das, A., Naylor, D.L., Breuer, K.S., 2023. Shape-Morphing Dynamics of Soft Compliant Membranes for Drag and Turbulence Modulation. *Physical Review Letters* 131, 114003. URL: <https://link.aps.org/doi/10.1103/PhysRevLett.131.114003>, doi:10.1103/PhysRevLett.131.114003. number: 11.
- Merritt, H., 1967. *Hydraulic Control Systems*. John Wiley & Sons, New York.
- Michel, S., Zhang, X.Q., Wissler, M., Löwe, C., Kovacs, G., 2010. A comparison between silicone and acrylic elastomers as dielectric materials in electroactive polymer actuators. *Polymer International* 59, 391–399. URL: <https://onlinelibrary.wiley.com/doi/10.1002/pi.2751>, doi:10.1002/pi.2751. number: 3.
- Miller, R.W., 1996. *Flow measurement engineering handbook*. 3rd ed ed., McGraw-Hill, New York.

- Murata, S., Tanaka, S., 1989. Aerodynamic characteristics of a two-dimensional porous sail. *Journal of Fluid Mechanics* 206, 463–475. URL: https://www.cambridge.org/core/product/identifier/S0022112089002363/type/journal_article, doi:10.1017/S0022112089002363.
- Nepf, H.M., 2012. Flow and Transport in Regions with Aquatic Vegetation. *Annual Review of Fluid Mechanics* 44, 123–142. URL: <https://www.annualreviews.org/doi/10.1146/annurev-fluid-120710-101048>, doi:10.1146/annurev-fluid-120710-101048. number: 1.
- Nia, H., Han, L., Li, Y., Ortiz, C., Grodzinsky, A., 2011. Poroe-
lasticity of Cartilage at the Nanoscale. *Biophysical Journal* 101, 2304–2313. URL: <https://linkinghub.elsevier.com/retrieve/pii/S0006349511010654>, doi:10.1016/j.bpj.2011.09.011. number: 9.
- Pinker, R.A., Herbert, M.V., 1967. Pressure loss Associated with Compressible flow through Square-Mesh wire Gauzes. *Journal of Mechanical Engineering Science* 9, 11–23. URL: http://journals.sagepub.com/doi/10.1243/JMES_JOUR_1967_009_004_02, doi:10.1243/JMES_JOUR_1967_009_004_02. number: 1.
- Roche, E.T., Wohlfarth, R., Overvelde, J.T.B., Vasilyev, N.V., Pigula, F.A., Mooney, D.J., Bertoldi, K., Walsh, C.J., 2014. A Bioinspired Soft Actuated Material. *Advanced Materials* 26, 1200–1206. URL: <https://onlinelibrary.wiley.com/doi/10.1002/adma.201304018>, doi:10.1002/adma.201304018. number: 8.
- Santhanakrishnan, A., Robinson, A.K., Jones, S., Lowe, A., Gadi, S., Hedrick, T.L., Miller, L.A., 2014. Clap and fling mechanism with interacting porous wings in tiny insect flight. *Journal of Experimental Biology* , jeb.084897 URL: <https://journals.biologists.com/jeb/article/doi/10.1242/jeb.084897/257605/Clap-and-fling-mechanism-with-interacting-porous>, doi:10.1242/jeb.084897.
- Sasso, M., Palmieri, G., Chiappini, G., Amodio, D., 2008. Characterization of hyperelastic rubber-like materials by biaxial and uniaxial stretching tests based on optical methods. *Polymer Testing* 27, 995–1004. URL: <https://>

- linkinghub.elsevier.com/retrieve/pii/S0142941808001529, doi:10.1016/j.polymertesting.2008.09.001. number: 8.
- Shian, S., Bertoldi, K., Clarke, D.R., 2015. Dielectric Elastomer Based “Grippers” for Soft Robotics. *Advanced Materials* 27, 6814–6819. URL: <https://onlinelibrary.wiley.com/doi/10.1002/adma.201503078>, doi:10.1002/adma.201503078. number: 43.
- Song, A., Tian, X., Israeli, E., Galvao, R., Bishop, K., Swartz, S., Breuer, K., 2008. Aeromechanics of Membrane Wings with Implications for Animal Flight. *AIAA Journal* 46, 2096–2106. URL: <https://arc.aiaa.org/doi/10.2514/1.36694>, doi:10.2514/1.36694. number: 8.
- Steeb, H., Renner, J., 2019. Mechanics of Poro-Elastic Media: A Review with Emphasis on Foundational State Variables. *Transport in Porous Media* 130, 437–461. URL: <http://link.springer.com/10.1007/s11242-019-01319-6>, doi:10.1007/s11242-019-01319-6. number: 2.
- Tiomkin, S., Raveh, D.E., 2021. A review of membrane-wing aeroelasticity. *Progress in Aerospace Sciences* 126, 100738. URL: <https://linkinghub.elsevier.com/retrieve/pii/S0376042121000439>, doi:10.1016/j.paerosci.2021.100738.
- Venkataraman, D., Bottaro, A., Govindarajan, R., 2014. A minimal model for flow control on an aerofoil using a poro-elastic coating. *Journal of Fluids and Structures* 47, 150–164. URL: <https://linkinghub.elsevier.com/retrieve/pii/S0889974614000280>, doi:10.1016/j.jfluidstructs.2014.02.012.
- Vogel, S., 1984. Drag and Flexibility in Sessile Organisms. *American Zoologist* 24, 37–44. URL: <https://academic.oup.com/icb/article-lookup/doi/10.1093/icb/24.1.37>, doi:10.1093/icb/24.1.37. number: 1.
- Vogel, S., 1989. Drag and Reconfiguration of Broad Leaves in High Winds. *Journal of Experimental Botany* 40, 941–948. URL: <https://academic.oup.com/jxb/article-lookup/doi/10.1093/jxb/40.8.941>, doi:10.1093/jxb/40.8.941. number: 8.
- Whitesides, G.M., 2018. Soft Robotics. *Angewandte Chemie International Edition* 57, 4258–4273. URL: <https://onlinelibrary.wiley.com/doi/10.1002/anie.201800907>, doi:10.1002/anie.201800907. number: 16.